Observation of chromatic effects in high-order harmonic generation

Xiaomeng Liu ⬤,[*] Antonios Pelekanidis ⬤,[*] Mengqi Du ⬤, Fengling Zhang ⬤, Kjeld S. E. Eikema ⬤, and Stefan Witte ⬤[†]

Advanced Research Center for Nanolithography, Science Park 106, 1098 XG Amsterdam, The Netherlands
and Department of Physics and Astronomy, LaserLaB, Vrije Universiteit Amsterdam,
De Boelelaan 1081, 1081 HV Amsterdam, The Netherlands

High-harmonic generation sources can produce coherent, broadband radiation at extreme-ultraviolet and soft-x-ray wavelengths. The wavefronts of the generated high-order harmonics are influenced by the incident laser field, the generation conditions, and geometry. These influences depend on harmonic wavelength, which may result in wavelength-dependent focusing properties and spatiotemporal couplings that can affect attosecond physics experiments. We experimentally demonstrate and characterize these chromatic effects in high-harmonic generation by measuring the spectrally resolved high-harmonic wavefronts as a function of generation conditions. We find that the high-harmonic generation process can have significant intrinsic chromatic aberration, particularly for converging incident laser fields. Furthermore, we identify regimes where chromatic effects can be minimized, and show that analytical single-atom models allow accurate predictions of harmonic wavefronts produced by a specific driving field.

I. INTRODUCTION

High-order harmonic generation (HHG) as a laboratory-scale source of coherent soft x-rays and extreme ultraviolet (EUV) pulses has become indispensable for many table-top coherent diffractive imaging (CDI) experiments [1–3], and attosecond physics [4]. In the high-harmonic generation process [5–8], an intense broadband femtosecond infrared laser pulse, with a peak intensity on the order of $10^{14} - 10^{15}\,\mathrm{W\,cm^{-2}}$, is focused into a noble gas medium. The strong driving field leads to electron tunneling, acceleration, and recombination, subsequently leading to the generation of a chirped broadband EUV pulse [4], which for multicycle laser pulses consists of a comb of odd-order harmonics of the drive laser frequency [9,10].

The ultrashort pulse duration and broad spectral bandwidth of HHG sources are key enabling features for probing ultrafast phenomena [11,12], but there is the possibility of couplings between their temporal and spatial properties [13]. Such spatiotemporal couplings can significantly increase the pulse duration upon propagation [14,15], affect the propagation itself in dispersive nonlinear media [16], and have an influence on nonlinear effects [17]. In the case of time-varying polarization states, spatiotemporal couplings become even more complex [18]. In many experiments in attosecond spectroscopy [19,20] and lensless imaging [3,21], a high quality

focus is crucial to obtain a short pulse duration and high peak intensity at the target.

While spatiotemporal coupling is typically associated with aberrations caused by optical components, recent work showed that the HHG process itself may already introduce chromatic aberrations [22–24], as the wavefront and intensity profile of the generated high-harmonic beam can depend both on the harmonic order and the generation geometry. Placing the gas medium slightly before the waist of the driving laser beam was shown to result in an HHG beam in which the wavefronts range from diverging to converging for different harmonics [24,25].

The wavefront distribution of a high-harmonic field can be expressed as [22]

$$\Phi_q(r, z) = q\phi(r, z) + \Phi_i(r, z), \tag{1}$$

where $\phi(r, z)$ is the drive laser phase, q is the harmonic order, and $\Phi_i(r, z)$ is the atomic dipole phase [5,26]. While the dipole phase is commonly approximated as $\Phi_i = \alpha_q I$ with I the laser intensity [26–28], we take the expression derived by Guo *et al.* [22,29] that for the short trajectories takes the form $\Phi_i = \gamma_s(q\omega_l - \omega_p)/I$. In this expression, $\omega_p = I_p/\hbar$ is the frequency corresponding to the ionization energy I_p and $\gamma_s = a\omega_l^2$ with ω_l the laser frequency and a a constant. These two dipole phase expressions are mutually consistent when taking into account that the α_q parameter depends on harmonic order and intensity [29]. The $1/I$ model is insightful as its prefactor is a true constant at fixed ω_l, and provides an analytical expression for the phase properties of HHG fields. For an HHG beam with a Gaussian spatial intensity profile, the radius of curvature of the HHG wavefront can be obtained by approximating the phase with a polynomial expansion up to r^2 (considering only short trajectories), plus the wavefront

[*]These authors contributed equally to this work.
[†]witte@arcnl.nl
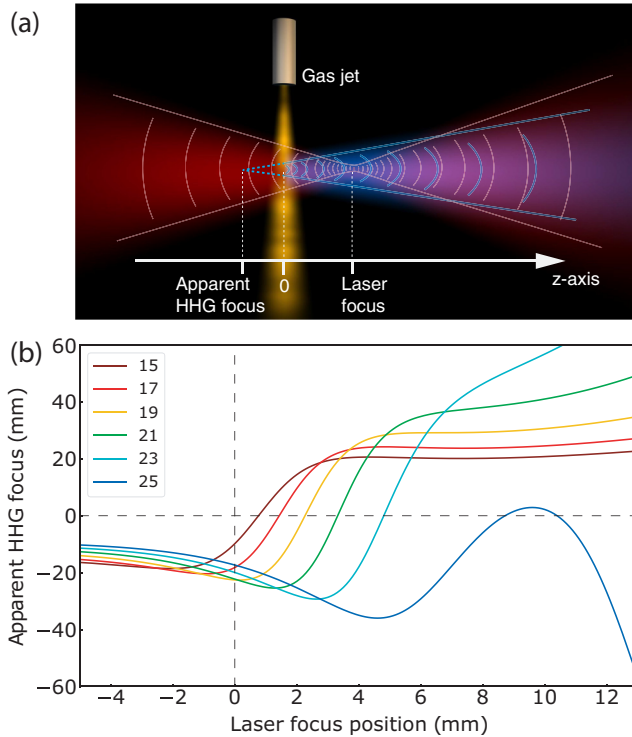
FIG. 1. (a) Typical geometry for high-harmonic generation (HHG). The wavefront curvature of the harmonics may differ from the driving field, mainly because of the dipole phase. (b) Apparent focus positions of harmonics 15–25 generated in Argon with laser parameters $\lambda = 800$ nm, $I_0 = 1.7 \times 10^{14}$ W/cm^2, $w_0 = 50$ μm. For both laser and HHG, positive numbers indicate a focus behind the gas jet (being a real HHG focus), and negative numbers mean the focus is before the jet (virtual HHG focus).

curvature of the drive laser [22]:

$$\frac{1}{R_q} = \frac{1}{R_l(z)} + \frac{4\gamma_s c(q\omega_l - \omega_p)^2}{I_0 w_0^2 q\omega_l},$$ (2)

in which $R_l(z)$ is the radius of curvature of the laser field at the gas jet, I_0 is the peak intensity, and w_0 is the beam waist.

Figure 1 shows the concept of the harmonics being generated with a different wavefront curvature than the driving field. We set the geometry as in Fig. 1(a), with the gas jet as the origin and positive z values being further downstream (behind the medium). The difference in wavefront curvature of the driving laser field leads to a different "apparent" focus position where the harmonics appear to originate from with significant dependence on the harmonic order [22,24]. We use Eq. (2) to calculate the expected apparent foci for our typical generation conditions, with the results shown in Fig. 1(b). In particular, for the laser focusing behind the gas jet, strong wavelength-dependent variations of several Rayleigh lengths in the HHG focus positions are predicted, with most harmonics changing from a virtual to a real focus at a specific generation position. Refocusing such beams for strong-field attosecond experiments would result in severe chromatic aberrations, even when using fully achromatic refocusing optics.

A quantitative experimental verification of these predicted chromatic aberrations is challenging, as it requires a

wavelength-resolved focus characterization with high spatial resolution. Alternatively, a model-independent reconstruction of the HHG focal spot is possible from high-resolution far-field measurements of the transverse complex field distribution of each harmonic. While various far-field wavefront sensing methods have been developed for HHG sources [23,30–34], achieving both sufficient spatial and spectral resolution without relying on model assumptions remained challenging. Recently, a computational imaging method called ptychography has been applied for wavefront sensing applications [3,35], where the quantitative complex electric field can be reconstructed with diffraction-limited spatial resolution. Specifically, for characterization of HHG sources, we have developed a multiwavelength ptychographic wavefront sensing (PWFS) method [36]. In this work, we employ PWFS to study the intrinsic chromatic variations in the HHG process with unprecedented detail. The reconstructed complex field distributions from PWFS can be numerically propagated back to their apparent focus position near the generation medium, without requiring Gaussian optics or assuming certain beam symmetry. By recording PWFS data as a function of the HHG generation geometry, a detailed analysis of these intrinsic chromatic effects in HHG becomes possible. By simultaneously characterizing the complex field of the drive laser, we can compare the measured HHG beams with single-atom-model predictions for a given driving field, enabling a critical comparison of different model approaches.

II. SETUP FOR PTYCHOGRAPHIC WAVEFRONT SENSING

We measure the multispectral EUV wavefronts and the fundamental laser wavefront with the experimental setup outlined in Fig. 2(a). High harmonics are generated in a gas jet, using 0.61 mJ, 45 fs, 825 nm wavelength laser pulses from a noncollinear optical chirped pulse amplifier running at 300 Hz repetition rate. The gas jet is formed by a supersonic expansion from a pulsed nozzle into a stainless steel tube with 0.6 mm inner diameter, at 2 bar Argon backing pressure. The laser crosses the jet through 100 μm diameter holes in the side of the tube. As the interaction length is significantly shorter than the 3.4 mm Rayleigh length of the laser focus, propagation effects are expected to be limited [28,37], and we therefore focus our analysis on the single atom response and the influence of the driving laser wavefront. For the PWFS measurements, an EUV wavefront sensor mask (EUV WFS), as used in [36], is mounted on a two-dimensional translation stage (Smaract SLC-1730) and placed 40.9 cm after the gas jet. A 200 nm thick free-standing aluminum filter blocks the fundamental beam, and the HHG beam is detected by an EUV-sensitive camera (Andor Ikon-L 936SO, 2048 × 2048 pixels, pixel size 13.5 μm) placed 56.5 cm behind the EUV WFS. A series of diffraction patterns is recorded as the EUV WFS is transversely scanned through the HHG beam. To characterize the fundamental field, a near-infrared ptychography measurement is set up in an auxiliary beam path outside the vacuum system. Band-pass filters are used to select single wavelengths from the driving laser, enabling characterization of the driving laser at several wavelengths across the broad spectrum. A different wavefront sensor mask is used to measure the fundamental wavefront [Fig. 2(b)]. An infrared camera (Allied
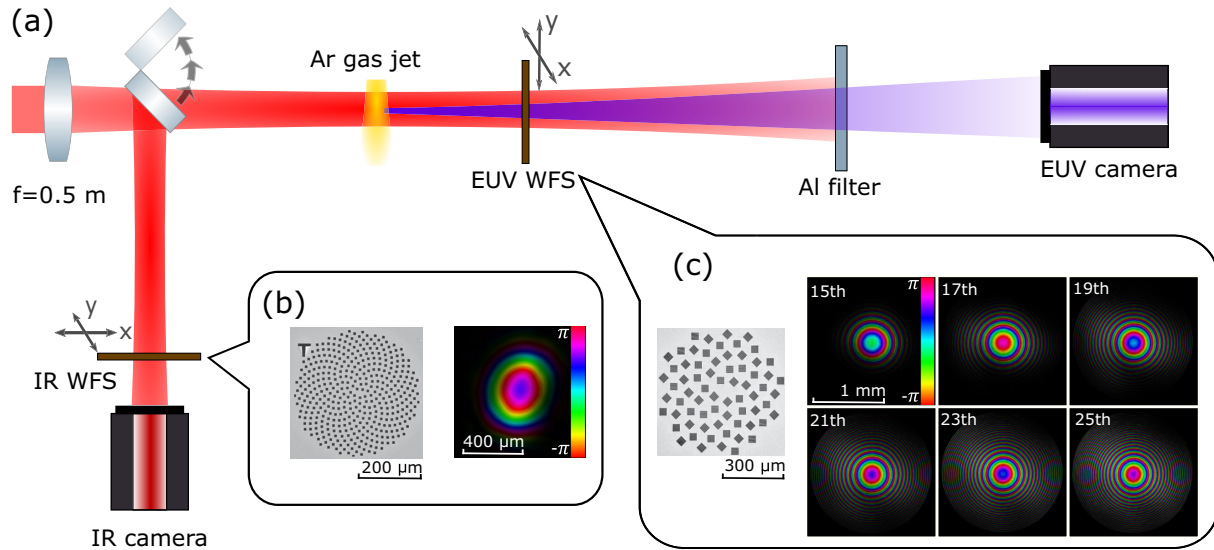
FIG. 2. (a) Experimental setup for wavelength-dependent EUV wavefront measurements. Ultrashort near-infrared pulses are focused into an Argon gas jet for HHG, using a $f = 0.5$ m lens. An EUV wavefront sensor mask (EUV WFS) is transversally scanned through the generated HHG beam for ptychographic wavefront characterization, and the resulting EUV diffraction patterns are recorded by an EUV-sensitive CCD camera. The fundamental field is also characterized using ptychography, in a separate measurement arm. (b) Scanning electron microscopy (SEM) image of the near-IR wavefront sensor mask, and a reconstructed laser field (brightness linearly encodes amplitude, color represents phase). (c) SEM image of the EUV WFS mask, and a set of reconstructed fields for different harmonics.

Vision Prosilica GT3400) is used to capture the diffraction patterns.

III. RESULTS: HHG WAVEFRONTS AND CHROMATIC ABERRATIONS

From a single ptychography scan, complex fields at all harmonic wavelengths are reconstructed [Fig. 2(c)]. These fields can be numerically propagated backward along the beam direction, enabling an accurate characterization of the focus position and the properties of the HHG beam [36].

A reconstruction result with an example of the numerical beam propagation for multiple harmonics is shown in Fig. 3. The first column [Figs. 3(a1)–3(a6)] contains the reconstructed multispectral EUV fields for harmonics 15 to 25 at the position of the EUV WFS. The plots in the middle column [Figs. 3(b1)–3(a6)] show the numerical propagation of the EUV beam through the beam waist, in which the beam direction is from left to right. The dashed white line indicates the position of the gas jet. It should be noted that only linear propagation is considered here, and any (nonlinear) effects of the gas jet on the beam propagation are not included. This approach provides a detailed view of the HHG beams around their focus region, with sufficient resolution to identify that the generated harmonics clearly have different focusing properties. In this example we find that the 15th harmonic focuses near the gas jet plane, while the higher harmonics show progressively larger divergence at the gas jet plane [Figs. 3(c1)–3(c6)], and have virtual foci up to several centimeters upstream of the jet. From the ptychography scans, the complex fields of the fundamental and the generated harmonics can be directly compared around the focus region.

To study the harmonic-order dependence of the focusing properties in detail, we performed a series of PWFS measurements while varying the relative position between the laser focus and the gas jet. The results are shown in Figs. 4(a) and 4(b) where the apparent focus position of harmonics 15 to 25 is determined as a function of the relative gas jet position. Due to slight astigmatism in the fundamental beam, we observed minor differences in horizontal and vertical focusing behavior; therefore we show separately the focus positions in the horizontal and vertical plane in Figs. 4(a) and 4(b), respectively.

In Fig. 4 we maintain the axis convention of Fig. 1, with positive numbers indicating a focus behind the gas jet (i.e., a real focus). The high resolution of our wavefront measurements enables an accurate determination of the focus position of the individual harmonics, with the major advantage that there are no assumptions needed to retrieve the focus position from the measured data, other than the paraxial approximation used in the numerical propagation of the fields. Therefore, we obtain a detailed overview of the intrinsic chromatic aberration resulting from the HHG process itself.

IV. DISCUSSION

The observed chromatic aberrations qualitatively follow the trends predicted by the single-atom model [Fig. 1(b)]. In the regime of HHG with a converging drive laser beam, some lower-order harmonics are found to have a real focus behind the jet [24]. For these harmonics, the fundamental wavefront contribution dominates the dipole phase. When the laser focus coincides with the gas jet, all harmonic wavefronts are diverging, as only the dipole phase contribution to the harmonic phase is present, which is always divergent. The harmonic-wavelength dependence of the dipole phase then directly results in chromatic variations. For a laser focus
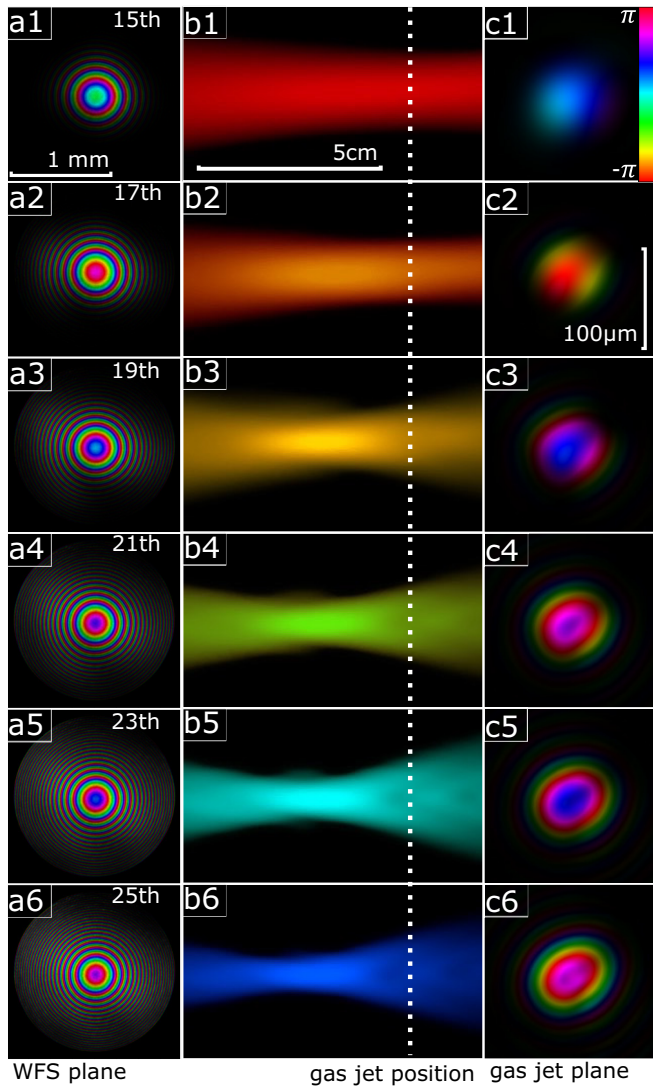
FIG. 3. (a) Reconstructed HHG wavefronts and focusing properties for a laser focus positioned 3.6 mm downstream of the jet. Left column (a1)–(a6): Reconstructed wavefronts of harmonic beams in the wavefront sensor plane. The corresponding wavelength (harmonic order) is 54.7 nm (15th), 48.2 nm (17th), 43.1 nm (19th), 38.9 nm (21st), 35.5 nm (23rd), and 32.6 nm (25th). Middle column (b1)–(b6): axial cross section of the reconstructed beam propagating through their foci. The scale bars are shared for all panels. The white dashed line indicates the gas jet position. Right column (c1)–(c6): reconstructed beam profiles in the gas jet plane. Intensity is linearly encoded in brightness, and phase is encoded as color.

before the jet, all harmonics have diverging wavefronts and thus virtual foci, as expected from Eq. (2). Note that these virtual harmonic foci are located several centimeters upstream of the laser focus. An important observation however, is that the chromatic aberrations are significantly smaller in this geometry. The origin of this behavior is that, while both the dipole phase and fundamental wavefront are diverging, their change as a function of harmonic order is largely inverse, thus
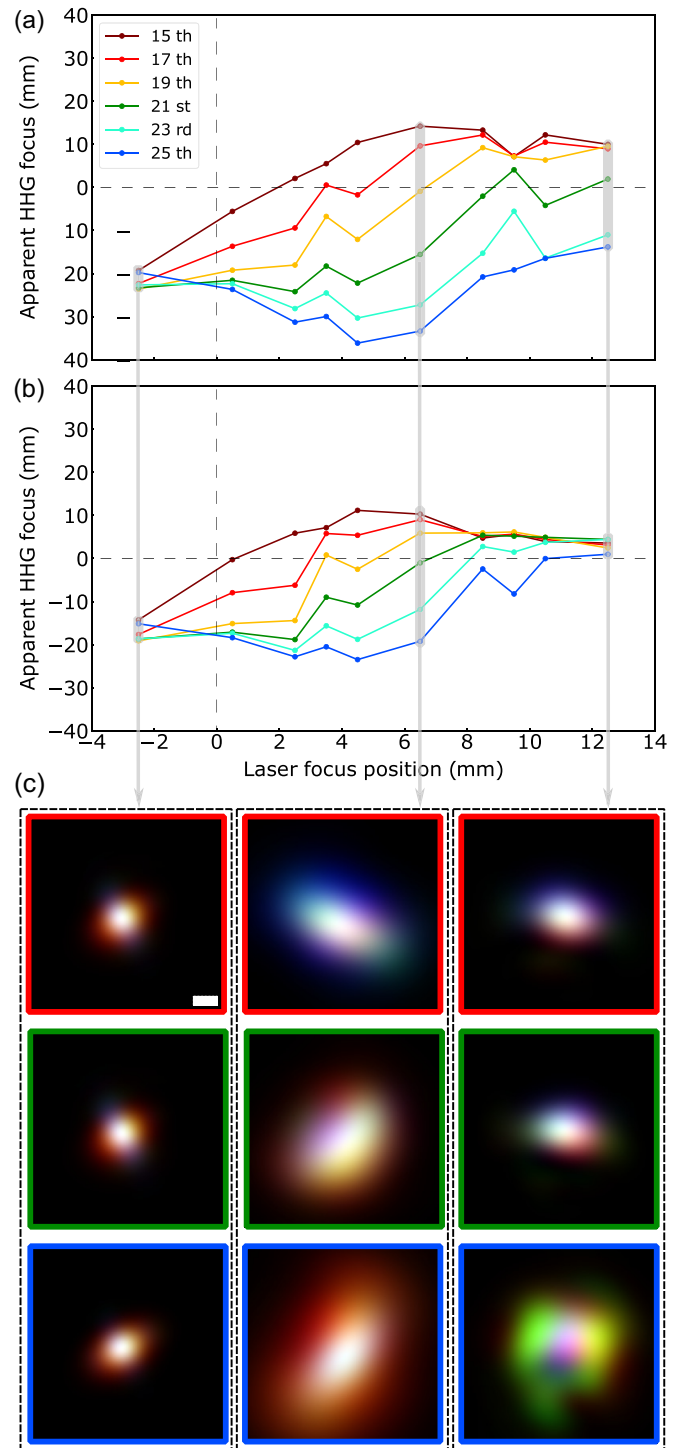
FIG. 4. (a), (b) Wavelength-dependent (a) horizontal and (b) vertical focus position of the different harmonics, as determined from reconstructed HHG wavefronts. (c) Overlay of reconstructed intensity profiles of harmonics 17 (red), 21 (green), and 25 (blue) at the apparent focus positions of the respective harmonics. The frame color indicates the harmonic that is in focus in that image (red H17, green H21, blue H25). The scale bar in the top left frame is 20 μm and is shared among all images.
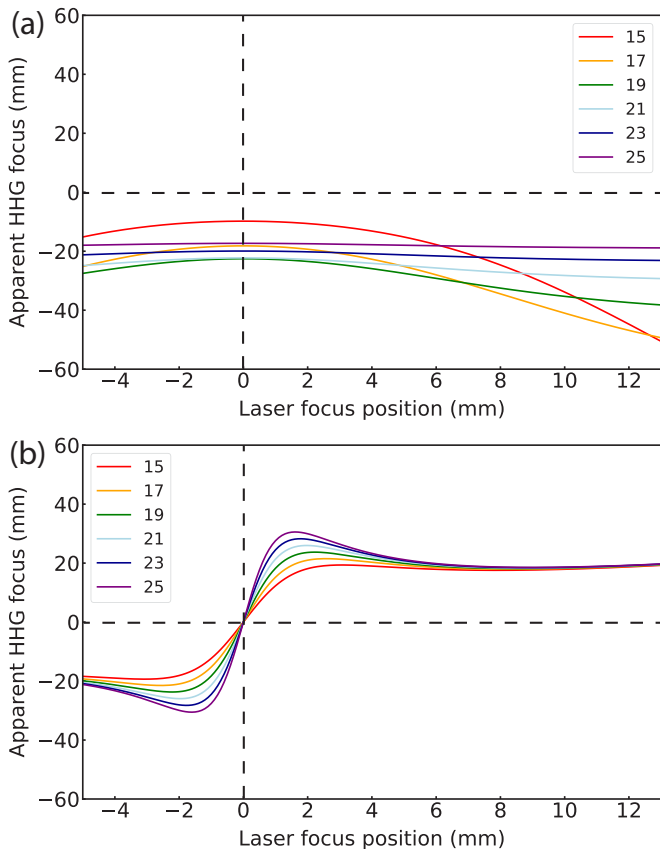
FIG. 5. Relative contributions to the wavefront and the resulting focus of the HHG beams. (a) The calculated apparent focus position only taking into account the dipole phase. (b) The calculated apparent focus without dipole phase, only considering transfer of the fundamental wavefront to the harmonics. Note that even for this contribution only, a chromatic effect appears. This is the result of the chosen waist size of the harmonics, which we set as $w_{\text{HHG}} = w_f(z)/\sqrt{m_{\text{eff}}}$ as discussed in the text. For an HHG waist size that scales as $w_f(z)/\sqrt{q}$, this chromatic effect in the phase transfer disappears.

partially canceling wavelength-dependent variations. Figure 5 shows the separate influence of dipole phase [Fig. 5(a)] and wavefront transfer [Fig. 5(b)].

By analyzing the reconstructed complex beam profiles, we find that the shift between the apparent HHG source positions of different harmonics can exceed the Rayleigh length of the harmonic beams in the present geometry by up to 2–4 times. This effect reaches a maximum when the laser focus is ~5 mm downstream of the gas jet, corresponding to about one fundamental Rayleigh length. Refocusing of such a multiwavelength beam, even with perfectly achromatic optics, will result in an aberrated focal spot with spatially varying spectral density and therefore similarly varying durations of attosecond pulses, following model predictions [22]. To give more direct insight into the beams produced in the HHG process, we numerically reconstruct the intensity profiles of three different harmonics around the generation region. The results are shown in Fig. 4(c), which contain the overlaid intensity profiles of harmonics 17, 21, and 25, at propagation distances that correspond to the apparent focus of each of

these harmonics, for three different fundamental focus positions. For a laser focus position before the gas jet, the apparent focus positions of all harmonics are almost identical, and we find a small HHG source spot with a similar profile for all harmonics. Moving to a laser focus behind the gas jet, where a large chromatic aberration was measured, we also observe significant differences in the intensity profiles of the respective harmonics: when reconstructing the HHG beam at the apparent focus position of one specific harmonic, the other harmonics appear clearly defocused, and there is no single position where all harmonics have identical profiles. Further details and additional visualizations are provided in Sec. 3 of Appendix. We previously already found that astigmatism transfers from the fundamental to the HHG beam in a wavelength dependent way [36], which is also observed in the present beam reconstructions. We now conclude that dipole-phase-induced wavefront curvature also leads to significant chromatic aberration, and this effect would remain even for diffraction-limited beams.

To connect these experimental results to expectations, a model is needed that simulates the properties of HHG fields based on fundamental field properties. The analytical single-atom model described by Eqs. (1) and (2) gives an expression for the wavefront, but not the intensity distribution, limiting the options for direct numerical propagation. To find the apparent focus position, the single-atom model does allow for a determination of the radius of curvature through Eq. (2). By approximating the beam properties in a Gaussian model, assuming a Gaussian intensity profile, and considering only quadratic phase profiles following the paraxial approximation, the focus position z of a beam can be calculated from the radius of curvature R and beam radius w at a given position along the beam propagation axis:

$$z_q = -\frac{R_q}{1 + \left(\lambda_q R_q / \pi w_q^2\right)^2}. \tag{3}$$

This Gaussian beam approach can be used when only HHG wavefront information is available, but does require an assumption for the waist of the generated HHG beam. In strong-field approximation (SFA) models, an effective nonlinearity m_{eff} is often assumed for plateau harmonics, resulting in a harmonic waist approximation as $w_{\text{HHG}} = w_f(z)/\sqrt{m_{\text{eff}}}$. For all our present single-atom model calculations we have taken $m_{\text{eff}} = 4$. Further details about the procedure to reconstruct the HHG focus position from the measured fundamental field are given in Sec. 1 of Appendix.

The high accuracy of the focus determination through ptychographic wavefront sensing enables a critical assessment of the dipole phase model. To this end, we calculate the single-atom model predictions using different approximations for the dipole phase, using the experimentally measured fundamental field as the starting point (Fig. 6). This field is numerically propagated to the gas jet plane, and its intensity and phase distributions serve as input to Eq. (1). This approach enables model predictions for astigmatic and otherwise aberrated beams, as often encountered experimentally. As the model does not include an estimate of the HHG efficiency, we assume Gaussian HHG intensity profiles when calculating the expected HHG focus position.
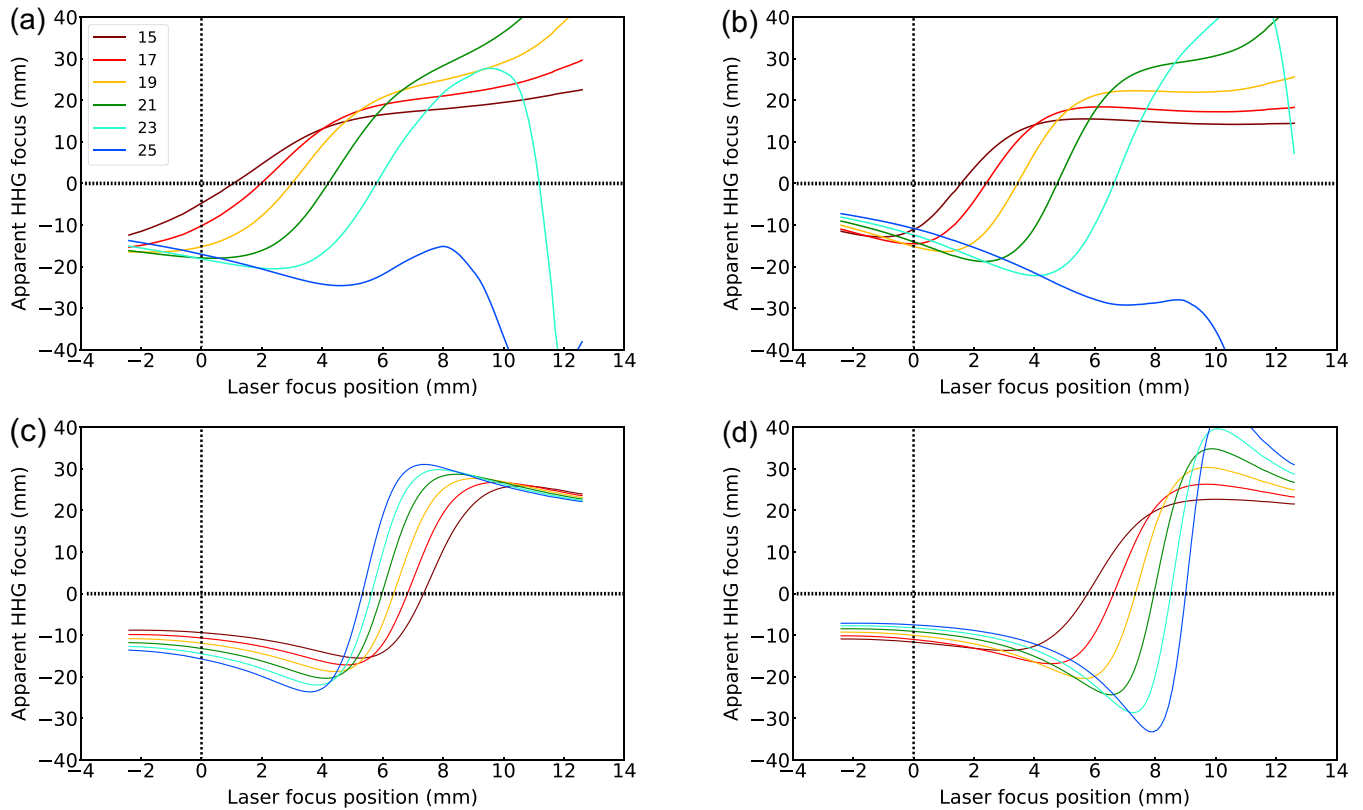
FIG. 6. Expected wavelength-dependent HHG focusing properties for different dipole phase models, based on the experimentally measured fundamental field. (a), (b) Calculated (a) horizontal and (b) vertical focus positions using the $\Phi_i \sim \gamma/I$ model, using $\gamma = 0.9569 \times 10^{-18}$ s^2 W/cm^2. (c) Calculation of horizontal focus positions using $\Phi_i \sim \alpha I$, taking a constant value $\alpha = -3 \times 10^{-14}$ cm^2/W. (d) Model with $\Phi_i \sim \alpha I$, taking $\alpha \sim q^2$, increasing from -2.025×10^{-14} at $q = 15$ to -7.225×10^{-14} at $q = 25$.

Figures 6(a) and 6(b) show the result for the horizontal and vertical focus positions, respectively, using the model introduced by Guo *et al.* [29] and Wikmark *et al.* [22], based on an analytical derivation resulting in a $1/I$ dependence for the dipole phase. These calculations show a high degree of similarity with the experimental results in Fig. 4. In Figs. 6(c) and 6(d) we plot the results of the horizontal focus positions for two other commonly used approaches to model the dipole phase, based on a $\Phi_i \sim \alpha I$ relation, in which the factor α is either constant [Fig. 6(c)] or quadratically proportional to harmonic order [Fig. 6(d)]. Note that in both cases, the values of α are chosen negative to ensure that the dipole phase adds a diverging wavefront curvature as physically expected. For the model with constant α, the chromatic aberrations are markedly different from the experimental observations. Making α dependent on harmonic order leads to a qualitative improvement, but this model significantly underestimates the magnitude of the chromatic aberrations when the gas jet is close to the laser focus, and predict variations around positive laser-gas jet positions that are not commensurate with the experimental results.

From this comparison we conclude that the $\Phi_i \sim \gamma/I$ dipole phase model provides an accurate description of the atomic response in our experimental geometry with a thin jet. While nonlinear propagation and phase matching effects

cannot be excluded, the close correspondence between the experimental results and simulations indicates that the observed chromatic effects are well-described by the single-atom response. Since our experiments are performed at high backing pressure, generating sufficient flux to collect the diffraction data needed in ptychographic imaging, self-focusing, and plasma-induced defocusing should be considered. For our experimental parameters, we estimate a B integral of 0.2, and an ionization level of 4% at the peak of the fundamental pulse. From these numbers we estimate that both self-focusing and plasma defocusing separately may lead to additional wavefront curvatures in the range $R \approx 5$–10 cm, and partially cancel as both effects have opposite signs. Such wavefront curvatures will not lead to significant shifts of the HHG foci, and are first order wavelength independent. Including such estimates in the calculations of Fig. 1(b) therefore only leads to a small horizontal shift of all the curves with respect to the laser focus position. Given the quantitative agreement between our single-atom calculations [Figs. 6(a) and 6(b)] and experimental observations [Figs. 4(a) and 4(b)], we conclude that for our parameters propagation-induced effects do not lead to significant modifications of the HHG focusing properties.

For HHG geometries with extended propagation length, more detailed simulations would be required for a quantitative analysis. However, the PWFS approach remains applicable to

experimentally characterize the resulting chromatic effects in the HHG beam.

V. CONCLUSION

In conclusion, we have experimentally demonstrated that the wavefronts of the HHG EUV beams can strongly depend on the wavefront and intensity profile of the fundamental laser, as well as the wavelengths of the harmonics themselves. We confirm that the $1/I$ model for the dipole phase can be used for realistic predictions of HHG wavefronts if a measured fundamental laser field is available. Our findings provide guidance for experiments that aim to tightly focus broadband attosecond pulses, where the effects of intrinsic chromatic aberration in the HHG process should be minimized.

APPENDIX

1. Calculating HHG focus position from fundamental beam reconstructions

As stated before, having the measured detailed complex field information for both the fundamental and the HHG beams enables a direct comparison, taking the effect of aberrations in the fundamental beam into account [36]. For the model predictions we initially calculate the phase of the high harmonic field at each frequency $q\omega_l$ according to Eq. (1), where the driving laser phase and intensity are known from the ptychographic characterization of the beam at a wavelength close to the central laser wavelength of 830 nm. By numerically propagating the reconstructed wavefront over a range of positions around the focus, we can simulate the high harmonic generation conditions for the different positions of the focusing lens.

From the estimated phase of the high harmonic wavefronts, we calculate the radius of curvature at the horizontal and vertical directions through fitting a quadratic curve on the 1D wavefront cuts. The radius of curvature for each direction is then

$$R_{x/y} = \frac{k_q}{2a_{2,x/y}}, \tag{A1}$$

FIG. 7. Beam diameter of the different harmonics at the gas jet position as reconstructed from the ptychography measurements for various distances between the gas jet and the fundamental beam waist position. (a) horizontal direction, (b) vertical direction.
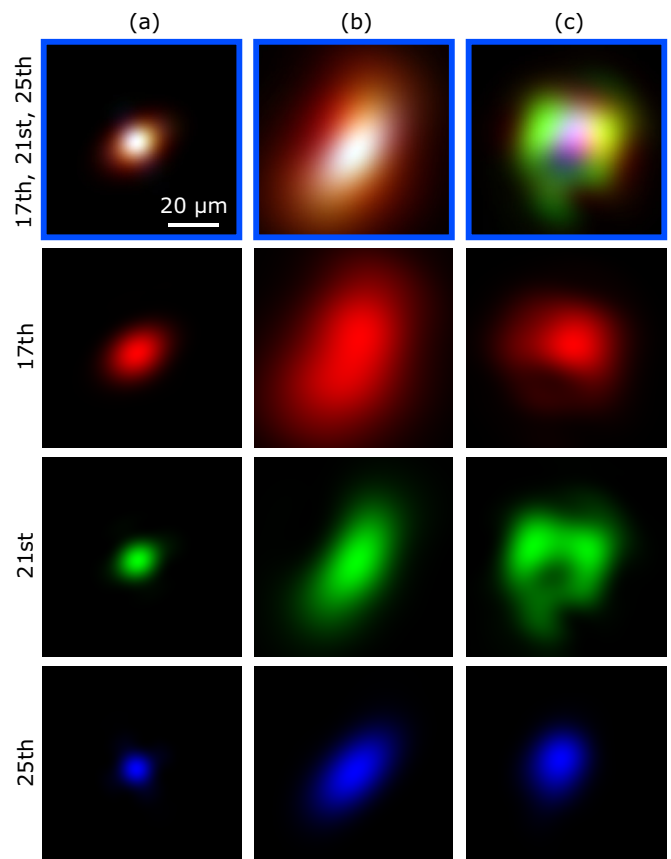
FIG. 8. Reconstructed beam profiles of harmonics 17, 21, and 25, both overlaid (top row) and separated, at the plane where harmonic 25 has its apparent focus for three different drive laser positions. The first row corresponds to the last row of Fig. 3 in the main text.

where k_q is the propagation number of the harmonic q, and a_2 is the quadratic term of the fitting curve. The focal distance can then be calculated directly from the radius of curvature using Eq. (3), which we apply for the x and y directions separately, with the assumption that $w_{HHG} = w_f(z)/\sqrt{m_{eff}}$.

To facilitate the quadratic fitting near the saddle point of the fundamental beam, we apply the fit separately to the two phase contributions $\Phi_1 = q\phi$ and $\Phi_2 = \Phi_i$. From these fits we get two radii of curvature per direction $R_{1,x/y}$ and $R_{2,x/y}$. The total radius of curvature then becomes

$$R_{x/y} = \left(\frac{1}{R_{1,x/y}} + \frac{1}{R_{2,x/y}} \right)^{-1}. \tag{A2}$$

The results from this process are equivalent to the results obtained when we fit a quadratic curve to the total HHG wavefront directly.

For the results shown in Figs. 6 we used a peak intensity at the fundamental beam waist of 2.3×10^{14} W/cm^2. At different gas jet positions, the peak intensity is scaled inversely proportional to the increase of the beam size and numerically calculated.

2. HHG beam diameters at the generation plane

As explained in the main text, the model used to estimate the intensity distribution of harmonics from a known fundamental field assumes a constant effective nonlinearity for plateau harmonics. Numerically propagating the measured harmonic fields to the source plane allows a verification of this assumption. From this data (Fig. 7), we actually find significant deviations from this SFA model waist assumption based on a constant effective nonlinearity. This discrepancy may limit the accuracy of a determination of the HHG wavefront based only on such model calculations, although we find that it does not change the conclusions for our experimental conditions.

3. Harmonic-resolved beam profile reconstructions

Figure 4(c) shows the reconstructed beam profiles of harmonics 17, 21, and 25 at different positions around the gas jet for three different generation positions. In those figures, the different harmonics are overlaid as RGB color plots. To provide a more detailed decomposition, we separate the channels of the bottom row of Fig. 4(c) and plot them together in Fig. 8. These are the beam profiles of the respective harmonics, back propagated to the position where harmonic 25 has its apparent focus. For the left column, which corresponds to a generation condition where the jet is positioned after the fundamental focus, little variation between the harmonics is observed and the spots are generally small. For conditions where the gas jet is placed before the laser focus [Figs. 8(b) and 8(c)], strong chromatic effects are observed. For large focus-jet separation [Fig. 8(c)], additional aberrations also become more apparent.

[1] G. S. M. Jansen, A. de Beurs, X. Liu, K. S. E. Eikema, and S. Witte, Diffractive shear interferometry for extreme ultraviolet high-resolution lensless imaging, Opt. Express **26**, 12479 (2018).

[2] R. L. Sandberg, A. Paul, D. A. Raymondson, S. Hädrich, D. M. Gaudiosi, J. Holtsnider, R. I. Tobey, O. Cohen, M. M. Murnane, H. C. Kapteyn, C. Song, J. Miao, Y. Liu, and F. Salmassi, Lensless diffractive imaging using tabletop coherent high-harmonic soft-x-ray beams, Phys. Rev. Lett. **99**, 098103 (2007).

[3] L. Loetgering, X. Liu, A. C. C. De Beurs, M. Du, G. Kuijper, K. S. E. Eikema, and S. Witte, Tailoring spatial entropy in extreme ultraviolet focused beams for multispectral ptychography, Optica **8**, 130 (2021).

[4] Y. Mairesse, A. De Bohan, L. J. Frasinski, H. Merdji, L. C. Dinu, P. Monchicourt, P. Breger, M. Kovacev, R. Taïeb, B. Carré, H. G. Muller, P. Agostini, and P. Salières, Attosecond synchronization of high-harmonic soft x-rays, Science **302**, 1540 (2003).

[5] M. Lewenstein, Ph. Balcou, M. Y. Ivanov, A. L'Huillier, and P. B. Corkum, Theory of high-harmonic generation by low-frequency laser fields, Phys. Rev. A **49**, 2117 (1994).

[6] K. J. Schafer, B. Yang, L. F. DiMauro, and K. C. Kulander, Above threshold ionization beyond the high harmonic cutoff, Phys. Rev. Lett. **70**, 1599 (1993).

[7] P. B. Corkum, Plasma perspective on strong field multiphoton ionization, Phys. Rev. Lett. **71**, 1994 (1993).

[8] K. Varju, P. Johnsson, J. Mauritsson, A. L'Huillier, and R. Lopez-Martens, Physics of attosecond pulses produced via high harmonic generation, Am. J. Phys. **77**, 389 (2009).

[9] F. Krausz and M. Ivanov, Attosecond physics, Rev. Mod. Phys. **81**, 163 (2009).

[10] P.-M. Paul, E. S. Toma, P. Breger, G. Mullot, F. Augé, Ph. Balcou, H. G. Muller, and P. Agostini, Observation of a train of attosecond pulses from high harmonic generation, Science **292**, 1689 (2001).

[11] A. H. Zewail, Femtochemistry: Atomic-scale dynamics of the chemical bond, J. Phys. Chem. A **104**, 5660 (2000).

[12] E. Goulielmakis, Z.-H. Loh, A. Wirth, R. Santra, N. Rohringer, V. S. Yakovlev, S. Zherebtsov, T. Pfeifer, A. M. Azzeer, M. F. Kling, S. R. Leone, and F. Krausz, Real-time observation of valence electron motion, Nature (London) **466**, 739 (2010).

[13] S. Akturk, X. Gu, P. Bowlan, and R. Trebino, Spatio-temporal couplings in ultrashort laser pulses, J. Opt. **12**, 093001 (2010).

[14] C. Bourassin-Bouchet, M. Stephens, S. de Rossi, F. Delmotte, and P. Chavel, Duration of ultrashort pulses in the presence of spatio-temporal coupling, Opt. Express **19**, 17357 (2011).

[15] C. Bourassin-Bouchet, M. M. Mang, F. Delmotte, P. Chavel, and S. de Rossi, How to focus an attosecond pulse, Opt. Express **21**, 2506 (2013).

[16] G. Cerullo, A. Dienes, and V. Magni, Space–time coupling and collapse threshold for femtosecond pulses in dispersive nonlinear media, Opt. Lett. **21**, 65 (1996).

[17] B. Beaurepaire, D. Guénot, A. Vernier, F. Böhle, M. Perrier, A. Jullien, R. Lopez-Martens, A. Lifschitz, and J. Faure, Limitations in ionization-induced compression of femtosecond laser

pulses due to spatio-temporal couplings, Opt. Express **24**, 9693 (2016).

[18] M. A. Porras, Propagation-induced changes in the instantaneous polarization state, phase, and carrier-envelope phase of few-cycle pulsed beams, J. Opt. Soc. Am. B **30**, 1652 (2013).

[19] A. L. Cavalieri, N. Müller, Th. Uphues, V. S. Yakovlev, A. Baltuška, B. Horvath, B. Schmidt, L. Blümel, R. Holzwarth, S. Hendel, M. Drescher, U. Kleineberg, P. M. Echenique, R. Kienberger, F. Krausz, and U. Heinzmann, Attosecond spectroscopy in condensed matter, Nature (London) **449**, 1029 (2007).

[20] M. Schultze, M. Fieß, N. Karpowicz, J. Gagnon, M. Korbman, M. Hofstetter, S. Neppl, A. L. Cavalieri, Y. Komninos, Th. Mercouris, C. A. Nicolaides, R. Pazourek, S. Nagele, J. Feist, J. Burgdorfer, A. M. Azzeer, R. Ernstorfer, R. Kienberger, U. Kleineberg, E. Goulielmakis, F. Krausz, and V. S. Yakovlev, Delay in photoemission, Science **328**, 1658 (2010).

[21] B. Zhang, D. F. Gardner, M. H. Seaberg, E. R. Shanblatt, C. L. Porter, R. Karl, C. A. Mancuso, H. C. Kapteyn, M. M. Murnane, and D. E. Adams, Ptychographic hyperspectral spectromicroscopy with an extreme ultraviolet high harmonic comb, Opt. Express **24**, 18745 (2016).

[22] H. Wikmark, C. Guo, J. Vogelsang, P. W. Smorenburg, H. Coudert-Alteirac, J. Lahl, J. Peschel, P. Rudawski, H. Dacasa, S. Carlström, S. Maclot, M. B. Gaarde, P. Johnsson, C. L. Arnold, and A. L'Huillier, Spatiotemporal coupling of attosecond pulses, Proc. Natl. Acad. Sci. USA **116**, 4779 (2019).

[23] E. Frumker, G. G. Paulus, H. Niikura, A. Naumov, D. M. Villeneuve, and P. B. Corkum, Order-dependent structure of high harmonic wavefronts, Opt. Express **20**, 13870 (2012).

[24] L. Quintard, V. Strelkov, J. Vabek, O. Hort, A. Dubrouil, D. Descamps, F. Burgy, C. Péjot, E. Mével, F. Catoire, and E. Constant, Optics-less focusing of XUV high-order harmonics, Sci. Adv. **5**, eaau7175 (2019).

[25] M. Hoflund, J. Peschel, M. Plach, H. Dacasa, K. Veyrinas, E. Constant, P. Smorenburg, H. Wikmark, S. Maclot, C. Guo, C. Arnold, A. L'Huillier, and P. Eng-Johnsson, Focusing properties of high-order harmonics, Ultrafast Science **2021**, 9797453 (2021).

[26] M. Lewenstein, P. Salières, and A. L'Huillier, Phase of the atomic polarization in high-order harmonic generation, Phys. Rev. A **52**, 4747 (1995).

[27] M. B. Gaarde, F. Salin, E. Constant, Ph. Balcou, K. J. Schafer, K. C. Kulander, and A. L'Huillier, Spatiotemporal separation of high harmonic radiation into two quantum path components, Phys. Rev. A **59**, 1367 (1999).

[28] F. Catoire, A. Ferré, O. Hort, A. Dubrouil, L. Quintard, D. Descamps, S. Petit, F. Burgy, E. Mével, Y. Mairesse, and E. Constant, Complex structure of spatially resolved high-order-harmonic spectra, Phys. Rev. A **94**, 063401 (2016).

[29] C. Guo, A. Harth, S. Carlström, Y.-C. Cheng, S. Mikaelsson, E. Mårsell, C. Heyl, M. Miranda, M. Gisselbrecht, M. B. Gaarde, K. J. Schafer, A. Mikkelsen, J. Mauritsson, C. L. Arnold, and A. L'Huillier, Phase control of attosecond pulses in a train, J. Phys. B: At. Mol. Opt. Phys. **51**, 034006 (2018).

[30] D. R. Austin, T. Witting, C. A. Arrell, F. Frank, A. S. Wyatt, J. P. Marangos, J. W. G. Tisch, and I. A. Walmsley, Lateral shearing interferometry of high-harmonic wavefronts, Opt. Lett. **36**, 1746 (2011).

[31] D. T. Lloyd, K. O'Keeffe, and S. M. Hooker, Complete spatial characterization of an optical wavefront using a variable-separation pinhole pair, Opt. Lett. **38**, 1173 (2013).

[32] D. G. Lee, J. J. Park, J. H. Sung, and C. H. Nam, Wave-front phase measurements of high-order harmonic beams by use of point-diffraction interferometry, Opt. Lett. **28**, 480 (2003).

[33] P. Mercère, P. Zeitoun, M. Idir, S. L. Pape, D. Douillet, X. Levecq, G. Dovillaire, S. Bucourt, K. A. Goldberg, P. P. Naulleau, and S. Rekawa, Hartmann wave-front measurement at 13.4 nm with λ_{EUV}/120 accuracy, Opt. Lett. **28**, 1534 (2003).

[34] L. Freisem, G. S. M. Jansen, D. Rudolf, K. S. E. Eikema, and S. Witte, Spectrally resolved single-shot wavefront sensing of broadband high-harmonic sources, Opt. Express **26**, 6860 (2018).

[35] M. Du, L. Loetgering, K. S. E. Eikema, and S. Witte, Measuring laser beam quality, wavefronts, and lens aberrations using ptychography, Opt. Express **28**, 5022 (2020).

[36] M. Du, X. Liu, A. Pelekanidis, F. Zhang, L. Loetgering, P. Konold, C. L. Porter, P. Smorenburg, K. S. E. Eikema, and S. Witte, High-resolution wavefront sensing and aberration analysis of multi-spectral extreme ultraviolet beams, Optica **10**, 255 (2023).

[37] A. L'Huillier, P. Balcou, S. Candel, K. J. Schafer, and K. C. Kulander, Calculations of high-order harmonic-generation processes in xenon at 1064 nm, Phys. Rev. A **46**, 2778 (1992).